Simulated Electron Affinity Tuning in Metal-Insulator-Metal (MIM) Diodes

Kissan Mistry[1,2], Mustafa Yavuz[1,2], Kevin Musselman[1,2]

[1]*Mechanical and Mechatronics Engineering, University of Waterloo, Waterloo, N2L 3G1, Canada*

[2]*Waterloo Institute of Nanotechnology, University of Waterloo, Waterloo, N2L 3G1, Canada*

Metal-Insulator-Metal (MIM) diodes for rectification applications must exhibit high asymmetry, nonlinearity and responsivity. Traditional methods of improving these figures of merit have consisted of increasing insulator thickness, adding multiple insulator layers and utilizing a variety of metal contact combinations. However, these methods have come with the price of increasing the diode resistance and ultimately limiting the operating frequency to well below the terahertz regime. In this work, an Airy Function Transfer Matrix simulation method was used to observe the effect of tuning the electron affinity of the insulator as a technique to decrease the diode resistance. It was shown that a small increase in electron affinity can result in a resistance decrease in upwards of five orders of magnitude, corresponding to an increase in operating frequency on the same order. Electron affinity tuning has minimal effect on the diode figures of merit, where asymmetry improves or remains unaffected and slight decreases in nonlinearity and responsivity are likely to be greatly outweighed by the improved operating frequency of the diode.

I. INTRODUCTION

A Metal-Insulator-Metal (MIM) diode is a nanoelectronic device that consists of a thin insulating dielectric sandwiched between two metal contacts. In recent years, these highly versatile devices have gained popularity for their applications in infrared detection[1,2], wireless power transmission[3,4] and solar energy harvesting[3,5–7]. The increasing demand for high speed electronics with small physical footprints has brought a focus on MIM diodes, which are advantageous due to their fast quantum tunneling conduction mechanism capable of operating at terahertz (THz) frequencies.

In any application, the main objective of the MIM diode is to rectify a high frequency AC signal to DC. The ideal diode current-voltage (IV) characteristic calls for an exponential behavior with high current at forward biases compared to the low 'near-zero' current at reverse biases. Three metrics have been defined to characterize a diode's rectification performance and are referred to as the Figures of Merit (FOM)[3] listed in Table I. The FOM quantitatively describe the nonlinear nature of a diode's IV response, where attaining the highest possible FOM corresponds to a diode capable of efficient rectification. Asymmetry is the ratio of forward current to reverse current, where values larger than 1 indicate rectification. Nonlinearity indicates the degree of sharpness in the turn on region of the IV curve. Lastly, Responsivity is a measure of DC current generated per unit of AC power.

TABLE I. MIM Diode Figures of Merit

Asymmetry	$f_{asym}(V) = \left\lvert \frac{I_F(V)}{I_R(V)} \right\rvert$
Nonlinearity	$f_{NL}(V) = \frac{\frac{dI}{dV}(V)}{\frac{I(V)}{V}}$
Responsivity	$f_{RES}(V) = \frac{\frac{d^2I}{d^2V}(V)}{\frac{dI}{dV}(V)}$

Current challenges in MIM diode design are associated with the goal of attaining THz rectification, where emphasis has been placed on obtaining diodes with high FOM. Research into improving the FOM has involved exploring a variety of material combinations[8–10], geometries[11–13] and fabrication methods[1, 3,14]. It is widely reported that the choice of metal contacts is critical for diode performance, where a large difference in work functions of the metals is desired to achieve high FOM[8,9,15,16]. Periasamy *et al.* implemented a high throughput screening technique to study a variety of metal-insulator combinations resulting in a device exhibiting the highest reported FOM[9] ($f_{asym} = 1500, f_{NL} = 4, f_{RES} = 20\ V^{-1}$), although the frequency response was not examined. A novel diode structure reported by Shin *et al.* implemented a multi-walled carbon nanotube (MWCNT) as one of the metal contacts[10]. The COMSOL simulation of the metal-insulator-MWCNT structure reported a cut-off frequency of 6.47 THz, however it was only capable of up to 10 MHz rectification experimentally. Along with the choice of metals, the properties of the insulator layer remain key parameters in diode design. With their high throughput screening technique, Periasamy *et al.* outlined the requirements of the insulator regarding the value of its electron affinity (χ_A) with respect to the metal work functions (ψ)[8]. Hashem *et al.*[16] demonstrated that increasing the insulator thickness and metal work function difference has a positive influence on the diode FOM. Furthermore, Alimardani *et al.* has thoroughly investigated the impact of the insulator material on the conduction processes through the diode[17,18]. A common geometrical variant consisting of a double insulator structure (MIIM) was experimentally realized by Maraghechi *et al.* and obtained up to 10 times improvement in nonlinearity compared to a single insulator diode with the same electrodes, but again the diode resistance and hence operating frequency were not considered[13]. These methods and many more have been implemented to improve the FOM but this has often been achieved at the expense of increasing the diode resistance. Alongside the FOM, the resistance is another key property in evaluating the performance of the MIM diode. The cut off frequency ($f = \frac{1}{2\pi RC}$) is inversely proportional to resistance and therefore to attain high frequency operation, the resistance must be minimized[19]. An understanding of the design parameters and their influence on the diode output is critical to optimizing this trade-off between FOM and resistance. While the studies noted above have been beneficial in determining

the impact of the insulator material and thickness on MIM diode performance, the influence of the insulator's electron affinity on the diode FOM, resistance, and corresponding frequency response has not been systematically studied.

The electron affinity of the insulator influences the height of the potential barrier in a MIM diode, and lowering of the barrier is expected to encourage more electron flow and thus lower the diode resistance. The electron affinity of a material can often be tuned by doping, where introduction of impurities into a semiconductor or insulator can alter the size of the band gap by raising or lowering the conduction/valence band edges[20–28]. In insulator or semiconducting materials, doping is commonly achieved by atomic layer deposition[20,29–33], sputter deposition[34–37] and chemical vapor deposition[38–46]. Strain induced electron affinity tuning has also been reported for various materials, commonly for wide band gap perovskite material combinations[47–51]. Similarly in 2D semiconductor materials, applied mechanical strains[52–54], lattice mismatch strains[55,56] and cation stearic size effects[57–59] have resulted in shifting of the conduction band. Notably, strain induced band gap tuning has been observed in thin films of titanium dioxide[60] and tin oxide[61]. The bandgap of quantum dots exhibit a particle size dependence[62–65], where band gap widening has been observed in quantum dots of zinc oxide[66,67] and titanium dioxide nanocrystals[68,69] . Further quantum dot band tuning is possible by surface modification with choice of ligand molecules[70]. Block copolymer films used in various flexible device applications, are able to exhibit electron affinity tuning over a broad range by varying the ratio of electron donor-acceptor units in the conjugated polymer film[71–73]. In this work, simulation of the diode IV characteristic was used to observe the effect of tuning the electron affinity of the insulator layer as a technique to optimize both MIM diode resistance and FOM.

II. BACKGROUND AND SIMULATION

The potential barrier in a MIM diode is defined by several parameters that pertain to the material selection and geometry of the diode. These parameters and the resulting barrier are depicted in Figure 1. The size and shape of the potential barrier directly affects the probability of electron tunneling and hence the diode FOM values. The width of the potential barrier is determined by the thickness and number of insulator layers. The height of the left and right sides (ϕ_L, ϕ_R) of the barrier are determined by the work functions of the metals (ψ_L, ψ_R) and the electron affinity of the insulator (χ_A). Two electron tunneling mechanisms are possible: direct tunneling and Fowler-Nordheim (FN) Tunneling[3]. Direct tunneling occurs when the tunnel current must travel across the entire width of the insulator. FN tunneling takes advantage of a reduced tunneling distance that arises in the triangular section atop the barrier as a result of the difference in metal work functions $\psi_R - \psi_L$ and applied bias (V_b), as shown in the inset of Figure 1. Conditions in which FN tunneling occurs, will produce higher current than the case of direct tunneling alone.

The left metal work function was selected to be smaller than the right metal work function $\psi_L < \psi_R$, such that a higher tunnelling current (forward current) occurs when the positive bias is applied on the right contact. This is due to higher electron tunneling probability arising from the smaller left barrier height (ϕ_L). It is intuitive to see that the large potential barrier on the right side (ϕ_R in Figure 1) impedes the flow of electrons. Thus, while the profile of the barrier encourages forward tunneling, its large size decreases the probability of reverse tunneling.

While conduction in MIM diodes is largely dominated by the femtosecond fast quantum tunneling processes[15,16], alternative conduction processes exist in dielectric thin films that must be considered. Notably, the electrode limited Schottky or thermionic emission and the bulk limited Poole-Frenkel (PF) emission[74–76]. Schottky emission is dependant on the barrier formed at the metal-insulator interface, where electrons with enough thermal energy can overcome the barrier. PF conduction occurs *via* trap states within the band structure due to defects in the insulator layer. In this work, simulations of the diode IV characteristic have been performed using the well established tunneling models, where Schottky and PF conduction have largely been neglected[7, 15,16,77]. However, for the case of electron affinity tuning, the impact of Schottky and PF emission should be considered. Electron affinity tuning will affect the magnitude of Schottky emission as it is directly dependent on the potential barrier height, and if tuning of the electron affinity is achieved by doping, an increased defect density can increase the probability of PF emission. The diode performance results presented herein have only considered tunneling conduction, however the conditions under which Schottky or PF emission may have a significant impact on the diode performance are discussed in detail in Section III.

It is also noted that electron conduction at metal-insulator interfaces results in a reduced "rounded-off" barrier known as the image charge potential, depicted in the Figure 1 (dotted line, ϕ_{image}). The image charge potential arises from the build up charge carriers at the metal-insulator interfaces and results in a rounding of the barrier edges[7, 15, 74, 76,78–82]. However the effects of the image charge potential have been omitted in the simulations presented here, as the decrease in the barrier height is expected to be minimal[79] and the effects negligible at high electric fields and ordinary temperatures[76,80]. Figure S1 in the supplementary material shows the effects of the image charge potential on the simulated current. The minimal reduction in barrier height results in a negligible increase in the diode current and is expected to have a negligible effect on the FOM calculated in this work. Furthermore, the omission of the image potential is supported by the close matching between simulation and experimental results shown elsewhere[7, 15,83].

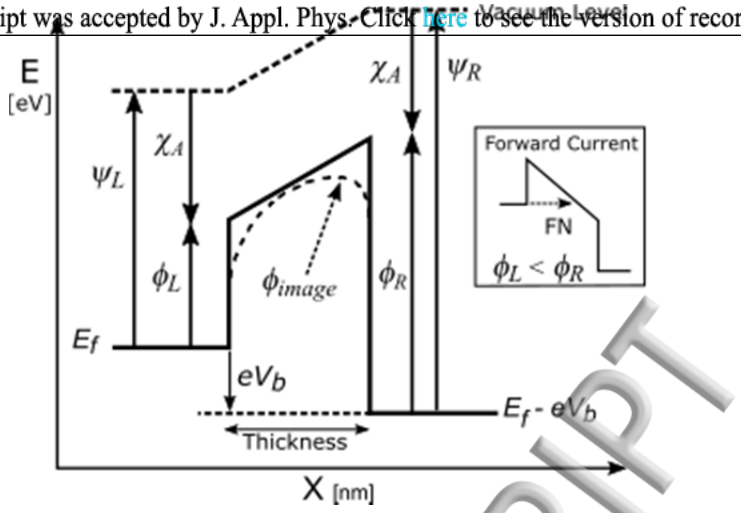

FIG. 1. MIM diode potential barrier construction as determined by metal work functions(ψ_L, ψ_R), insulator electron affinity (χ_A) and thickness. The barrier heights ($\phi_{L,R}$) are determined by the difference between the work function and electron affinity ($\psi_{L,R} - \chi_A$). The dotted line shows the shape of the image charge potential (ϕ_{image}) that has been neglected. With the left contact grounded, an applied bias (V_b) across the diode raises or lowers the fermi level (E_f) of the right metal in accordance to the direction of bias. The inset shows the energy level diagram when forward current occurs, where the lower left barrier height (ϕ_L) and Fowler-Nordheim (FN) tunneling promote higher current.

The electron tunnelling and resulting MIM diode IV characteristics were simulated with an Airy Function Transfer Matrix Method (AF-TMM), as reported by Hashem *et al.*[16] Inputs to the simulation such as the metal work functions, insulator electron affinity and thickness are used to construct the shape of the potential barrier. The AF-TMM solves the one-dimensional Schrodinger wave equation to determine transmission probability of the electron wave through the potential barrier. The transmission probability is combined with the Fermi-Dirac distributions to obtain the current density (A/cm^2) as a function of the applied bias voltage. The method reported by Hashem *et al.*[16], as well as other similar approaches[7, 15,77] that consider tunneling conduction, have shown good matching to experimental diode measurements. The diode FOM were calculated as listed in Table I, and the values at 2V were taken for comparison (similar FOM trends at 3V are presented in the supplementary material). A bias of 2V is used for comparison as it occurs after the turn on voltage of the majority of the simulated diodes. The diode resistance is an important property that is discussed herein and is calculated as the differential resistance $\left(\frac{\partial I}{\partial V}\right)^{-1}$ at zero bias. A parametric sweep of the diode parameters was done to observe their influence on the diode performance as discussed in the following section. The insulator thickness was swept from 4 nm to 10 nm, as the thickness should be kept lower than 10 nm for the tunneling conduction mechanism to dominate[84]. A variety of commonly deposited metals (aluminum, titanium, chromium, copper, gold and platinum) were simulated, effectively sweeping the work function difference between the two contacts $\psi_R - \psi_L$, from 0.05eV to 1.37eV. The work functions used for these metals are listed in Table II. Lastly, the electron affinity (χ_A) was swept from 2.6eV to 4.4eV, in steps of 0.2eV. Tuning the electron affinity across the entire range of simulated values (from one extreme to the other) would be difficult experimentally without greatly altering the material structure. Additionally, large range tuning by doping of the insulator could significantly increase the

defect density and result in a dominant PF conduction process instead of tunneling. Nonetheless, this broad range of electron affinities are considered in order to effectively present the trends discussed in the next section. However, it is emphasized that the conclusions in regards to the FOM made in Section III only concern the effects of electron affinity tuning by ±0.2eV, which is feasible to achieve experimentally with minimal change to the material structure[20–73]. Comparisons are made to the electron affinity of 3.8eV, which is similar to that of undoped titanium dioxide, a very common dielectric that has been doped in practise[60, 68,69,85–89].

TABLE II. Metals used in the simulation with respective work functions $\psi_{R,L}$.

Metals	Work Function $\boldsymbol{\psi_{L,R}}$ [eV]
Aluminum	4.28
Titanium	4.33
Chromium	4.50
Copper	4.70
Gold	5.10
Platinum	5.65

III. RESULTS AND DISCUSSION

The influence of the insulator thickness and metal work function difference ($\psi_R - \psi_L$) on the asymmetry FOM (measured at 2 V) was simulated and is shown in Figure 2 for an electron affinity of 3.8 eV. Aluminum was kept as the left work function ψ_L, while the right work function ψ_R was varied from the metals listed in Table II. As shown previously[16], the asymmetry increases as the insulator thickness and $\psi_R - \psi_L$ are increased. Furthermore, at larger $\psi_R - \psi_L$ the influence of increasing the thickness is amplified and allows for up to 10 orders of magnitude improvement in asymmetry. Similar trends were also observed for asymmetries calculated at different voltages.

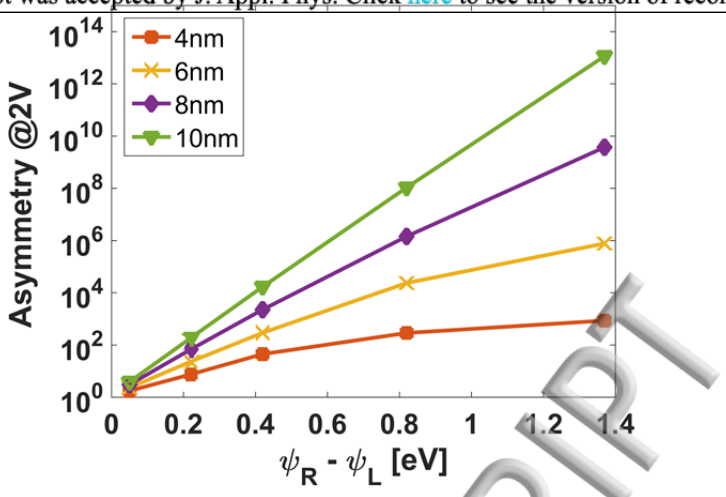

FIG. 2. Diode asymmetry as a function of increasing thickness and work function difference ($\psi_R - \psi_L$). Insulator electron affinity χ_A, is kept at 3.8eV. Aluminum was kept as the left work function ψ_L, while the right work function ψ_R was varied from the metals listed in Table II. Asymmetry is taken at 2V from the diode IV characteristic.

While increasing the thickness and $\psi_R - \psi_L$ of the diode are simple methods for improving the diode FOM, there lies an inherent drawback. As a result of the larger potential barrier (larger thickness or ϕ_R), the diode resistance increases and subsequently the magnitude of the rectified current produced is decreased. Figure 3a shows the differential resistance of the MIM diode with the same simulation parameters as Figure 2. The differential resistance is seen to increase as both the thickness and $\psi_R - \psi_L$ are increased. The inset of Figure 3a shows the potential barrier profiles for increasing $\psi_R - \psi_L$. As $\psi_R - \psi_L$ increases, the height of the right barrier, ϕ_R, increases. Although this higher barrier on the right side of the diode limits reverse bias current, it also increases the applied bias required to reach the FN tunnelling regime shown in the inset of Figure 1, thus limiting the forward bias current as well. Figure 3b displays the simulated current density at an applied (forward) bias of 2V for the same simulation parameters as Figures 2 and 3a. A significant decrease in current density with increasing insulator thickness and $\psi_R - \psi_L$ is clearly visible. Theoretically, these improved diodes have good rectification characteristics (high FOM) but become redundant if they cannot produce substantial rectified current. Applications in rectenna based energy harvesting or IR/UV detection will require high current output for improved efficiency and sensitivity. Consequently, a performance tradeoff is presented where the methods used to achieve good rectification (as defined by the FOM) result in higher resistance and limit the attainable operating frequency.

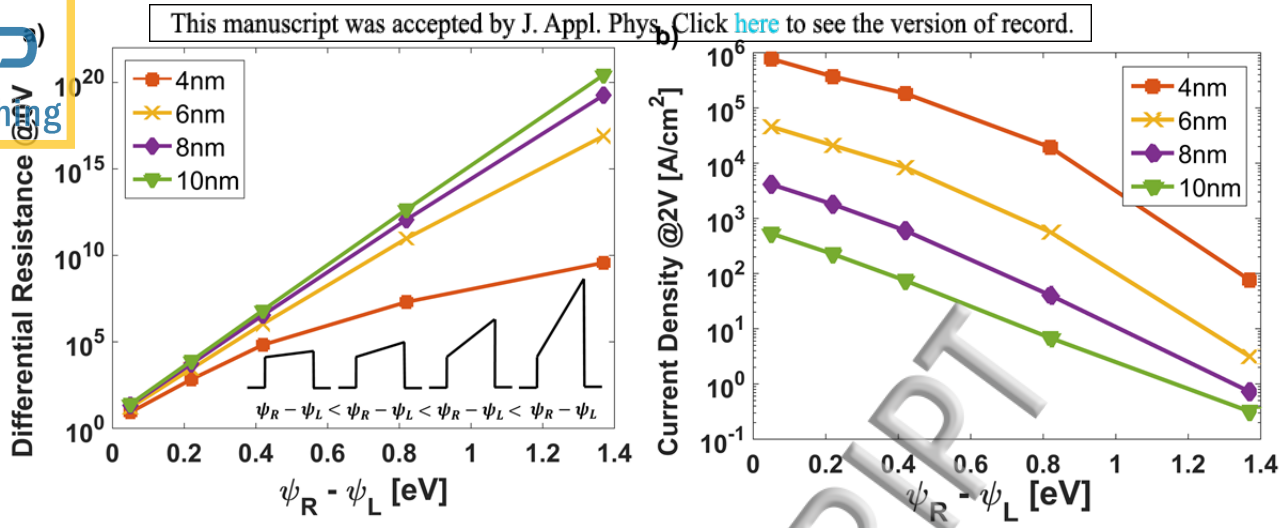

FIG. 3. The drawbacks from increasing MIM diode thickness and work function difference ($\psi_R - \psi_L$). a) Differential resistance and b) current density at 2V bias as a function of insulator thickness and $\psi_R - \psi_L$. Inset figure shows the shape of the potential barrier for increasing $\psi_R - \psi_L$ where the resistance increases due to the larger barrier heights.

As a potential solution to the discussed problem, the effects of tuning the electron affinity of the insulator layer were investigated. It is expected that lowering the height of the potential barrier will reduce the diode resistance[19]. This can be achieved on both sides of the barrier by increasing the electron affinity. Furthermore, this method of reducing the resistance does not affect $\psi_R - \psi_L$, preserving the profile of the triangular section atop the potential barrier and the conditions for Fowler Nordheim Tunneling. It was previously reported that the ideal MIM diode should have a low forward barrier height ($\phi_L = \psi_L - \chi_A$) and thus the electron affinity of the insulator and the work function of the left metal should be similar in value[8]. The need to find compatible metal-insulator combinations can be avoided by tuning the electron affinity of the insulator to a compatible value. Figure 4a shows the differential resistance of the diode as a function of electron affinity for different insulator thicknesses with the Al-Pt metal electrode combination ($\psi_R - \psi_L = 1.37eV$). Similar resistance data for other simulated metal combinations are shown in Figure S2 in the supplementary material. It is seen that increasing the electron affinity of the insulator layer resulted in a substantial reduction in diode resistance for all insulator thicknesses. The magnitude of the decrease was dependent on the thickness of the insulator layer, with greater reductions in resistance evident for the diodes with thick insulator layers. For the 4 nm thick diode, a resistance decrease on the order of 10^1 was observed for an +0.2eV increase in electron affinity. Whereas for the thicker diodes (6-10 nm) the resistance decrease was observed to be on the order of 10^2-10^5 in magnitude. Therefore, it can be stated that a small increase in electron affinity of 0.2eV has the potential to increase the operating frequency by 5 orders of magnitude. Figure 4b shows the simulated differential resistance of the diodes as a function of electron affinity for different $\psi_R - \psi_L$ and a fixed insulator thickness of 6nm. Similar resistance data for other thicknesses are shown in Figure S3 in the supplementary material. Again, a reduction in diode resistance is

observed with increasing electron affinity, but it is seen that different metal combinations generally had no effect on the magnitude of the resistance reduction.

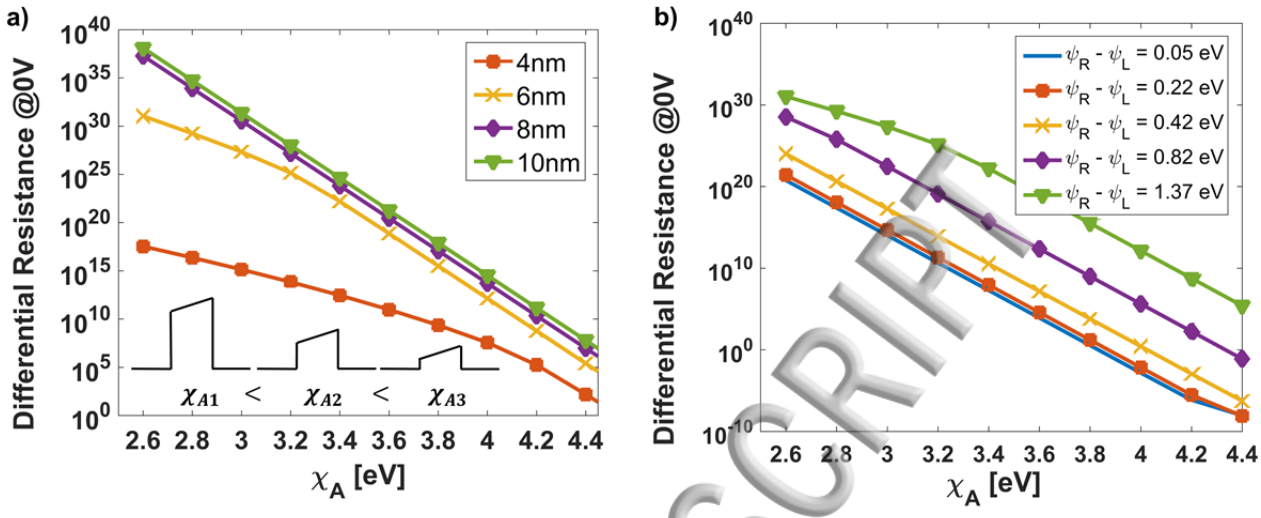

FIG. 4. Diode resistance as a function of electron affinity for a) an aluminum ($\psi_L = 4.28eV$) – platinum ($\psi_R = 5.65eV$) diode, (work function difference $\psi_R - \psi_L = 1.37eV$) with different insulator thicknesses and b) a diode with a 6nm thick insulator layer and different work function differences. Figures S2 and S3 in the Supplementary Material show similar resistance data for other simulated metal combinations and thicknesses. The inset figure shows the height of the barrier decrease for increasing χ_A, allowing for greater current flow and thus the reduced resistance.

The lower resistances observed in Figure 4 for higher insulator electron affinities follow directly from lower barrier heights, as illustrated schematically in the inset of Figure 4a, which induce a larger electron tunnelling probability. As a result, a significant increase in current density, on the same order of magnitude as the change in resistance, was observed as the electron affinity of the insulator was increased (refer to Figure S4 in the supplementary material). Consequently, a shift in the diode turn on voltage (TOV) towards lower voltages is observed as the electron affinity is increased, as shown in Figure 5 for an Al-Pt diode ($\psi_R - \psi_L = 1.37\ eV$) with a 6 nm thick insulator layer. TOV has been defined as the bias at which significant exponential increase in current is observed[18] and has been determined by the extrapolation in the linear region (ELR) method reported elsewhere[90]. The TOV is correlated to the onset of the Fowler-Nordheim (FN) tunneling regime. As demonstrated by the inset in Figure 5, at higher χ_A the FN tunneling regime is reached at lower voltages and thus a lower TOV is observed. This trend of decreasing TOV with increased insulator electron affinity was observed for a variety of relevant diode thicknesses and work function differences (refer to Figure S5 in the supplementary material).

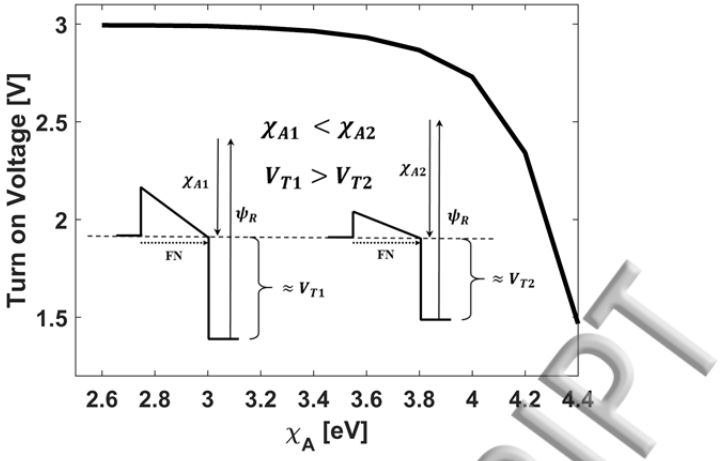

FIG. 5. Location of the turn on voltage (TOV) as the electron affinity (χ_A) of the insulator is increased for a 6 nm thick diode with aluminum and platinum electrodes ($\psi_R - \psi_L = 1.37\ eV$). Inset figure illustrates the TOV (V_T in figure) dependence on the height of the potential barrier, where lower TOVs are obtained at higher χ_A. The TOV is correlated to the voltage required to reach Fowler-Nordheim tunneling in the forward direction.

To be considered an effective technique for reducing MIM diode resistance, tuning of the insulator electron affinity (e.g., *via* insulator doping) must be justified by examining the influence on the diode FOM. The effect of adjusting the electron affinity by 0.2 eV on the asymmetry is shown in Figure 6. The asymmetry is shown as a function of $\psi_R - \psi_L$ for four different insulator thicknesses, as a comparison to the asymmetry shown earlier in Figure 2. A slight increase in the electron affinity from 3.8 eV to 4.0 eV does not have a negative effect on the asymmetry and in fact shows improvement for most insulator thicknesses and $\psi_R - \psi_L$. There is minimal change to asymmetry at low $\psi_R - \psi_L$ due to the inherently symmetric nature of the potential barrier. The forward and reverse tunnelling probabilities are influenced similarly by changes to the electron affinity. In contrast, potential barriers with larger $\psi_R - \psi_L$ have a prominent asymmetric shape and reduction of the barrier heights with increased electron affinity results in a larger relative increase in the forward tunnelling current than the reverse current, and hence a substantial increase in asymmetry. At low insulator thickness the electron affinity increase results in considerable improvement in asymmetry. This contrasts with the negligible change in asymmetry of the thicker 10nm diode, where the thickness of the potential barrier, rather than the barrier height, dominates the tunneling mechanism. Similar behavior is observed when the asymmetry is calculated at 3V, rather than 2V (refer to Figure S6 in the supplementary material). Asymmetry increase is welcomed, negligible change is acceptable, and minor decreases are mitigated by the substantial decrease in diode resistance observed for increasing electron affinity (Figure 4). These are all positive outcomes as the diode's capability to operate at higher frequency becomes feasible.

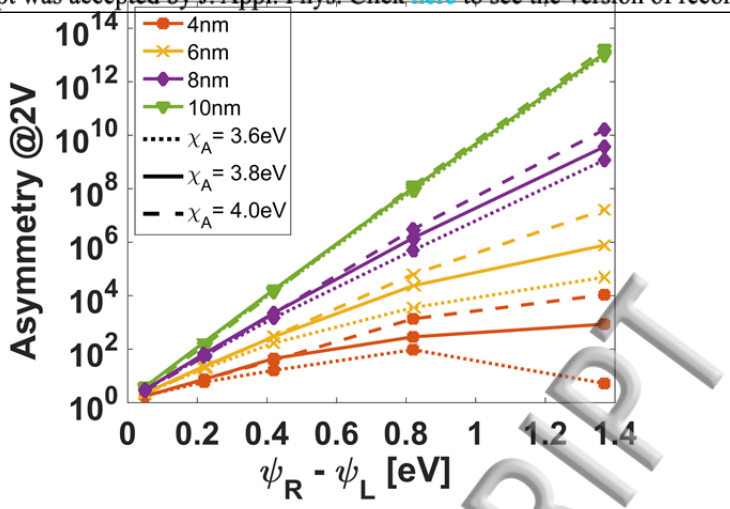

FIG. 6. Diode asymmetry as a function of increasing work function difference ($\psi_R - \psi_L$), for electron affinities of 3.6 eV, 3.8 eV, and 4.0 eV, and different insulator thicknesses. Figure S6 in the supplementary material presents similar trend for asymmetry taken at 3V

Figure 7 shows the simulated effect of electron affinity tuning on the nonlinearity and responsivity of a 6nm thick MIM diode as a function of increasing $\psi_R - \psi_L$. It is evident that increasing the electron affinity results in a slight decrease in both nonlinearity and responsivity. Unlike the change in asymmetry, the changes in both nonlinearity and responsivity for a 0.2 eV shift in the electron affinity are within one order of magnitude. Similar behaviour is seen for other insulator thicknesses (refer to Figures S7-S10 in the supplementary material). Depending on the application, these reductions in nonlinearity and responsivity for larger electron affinities are likely to be acceptable, given the large improvements in asymmetry, resistance and attainable operating frequency.

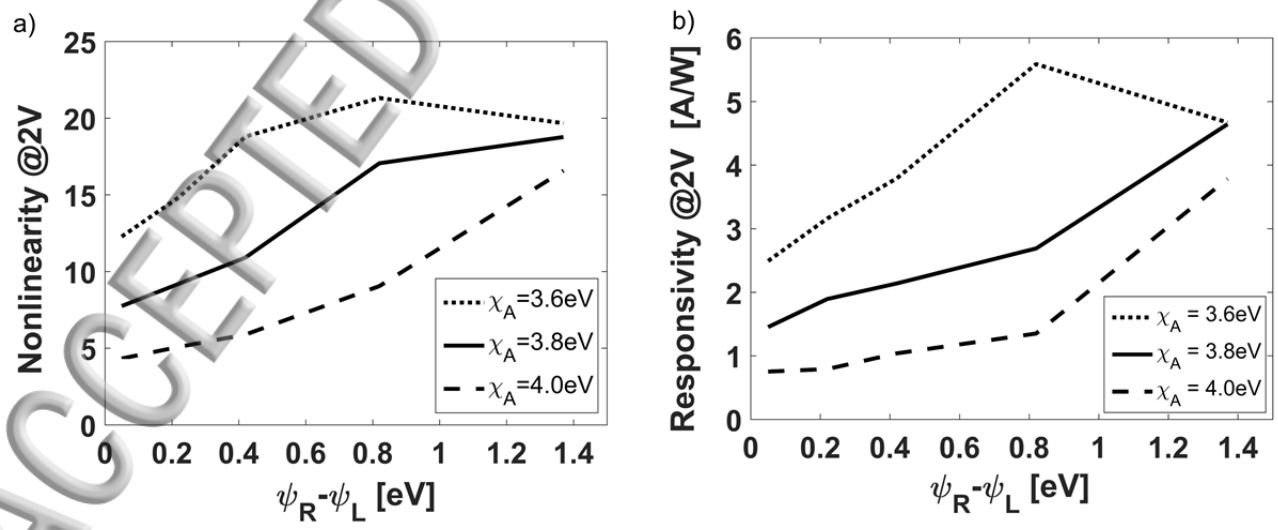

FIG. 7. Nonlinearity and responsivity of a simulated MIM diode with a 6nm thick insulator as a function of increasing work function difference ($\psi_R - \psi_L$) for three different electron affinities from 3.6eV to 4.0eV. Similar trend is observed at other thicknesses as shown in Supplementary Material Figures S7-S10.

It is important to note that experimentally, the behaviour of the diode can be greatly affected by the quality of fabrication, where defects in the film and poor metal-insulator interfaces can alter the IV characteristic from expected behavior[3, 9, 15, 18,81]. The impact of electrode surface on the diode current has been thoroughly studied[18,91–96]. Alimardani *et al.* reported that electrode roughness levels of less than 20% of the insulator thickness are desirable to achieve non-roughness dominated conduction in MIM diodes[91]. Crystallinity of the electrode surface can have a negative impact[95] where different orientation of grains results in work function non-uniformity[96]. Similarly, the crystallinity of the insulator may create alternate conduction paths, such that the current deviates from ideal behavior[97], and pinholes in the insulator can result in conduction that is orders of magnitude larger than tunnelling currents[7,15]. Furthermore, surface states due to chemical contamination (from fabrication) can alter the potential barrier heights and consequently the current[7]. Careful experimental investigation is therefore warranted to see whether the positive effects of electron affinity tuning observed in the simulations presented here can be achieved in practice. Atomic layer deposition (ALD) is capable of high quality, pinhole free thin films[98] and is commonly used for insulator deposition of MIM diodes as shown in several recent reports[7,8, 13, 17,84]. Furthermore, its ability to incorporate dopant atoms[20,29–33] makes ALD a good candidate for experimental investigations.

As previously mentioned, possible contributions of Schottky and PF conduction should be considered when simulating electron affinity tuning of the insulator. Schottky emission is dependent on the height of the potential barrier ($\phi_{L,R}$) formed at the metal-insulator interface[18,75]. Figure 8 compares calculated Schottky current to simulated tunneling current for an Al-TiO_2-Pt diode with a 6nm thick insulator layer. The model for the Schottky current has been reported in literature[75]. It is observed that the Schottky current dominates at lower biases before the TOV of the tunneling current, whereas the tunnelling current dominates beyond the TOV. Figure S11 in the supplementary material further shows the magnitude of the difference between Schottky and tunneling currents, where the difference between the two currents in the low bias regime is minimal (due to the low current magnitudes at low biases) and the tunnelling current is much larger at higher voltages. The FOM trends presented in this work have been determined at 2V, which is in proximity to the diode TOV and hence where tunneling is seen to begin dominating over Schottky conduction in Figure 8, such that the choice to consider only tunneling current is appropriate. For lower voltages, it is expected that the operation of the device would be fundamentally different, as tunnel current no longer dominates. Schottky current is also seen to be more prevalent at high electron affinities where the potential barrier is small, as shown in Figure 8 (as well as Figure S11 in the supplementary material) for $\chi_A = 4.2eV$. For these high χ_A diodes, the current density inclusive of Schottky current would be larger than that of tunnelling alone, and hence the resistance would be lower than as presented in Figure 4. The FOM for the Al-TiO_2-Pt diode with $\chi_A = 4.2eV$ were determined with Schottky current accounted for and are presented in Figure S12 in the

supplementary material. It is observed that the Schottky current FOM for high χ_A diodes are lower in magnitude compared to the FOM of tunneling current alone.

The consideration of Schottky reverse bias currents alters the diode asymmetry for larger $\psi_R - \psi_L$. Both tunneling and Schottky currents are 'near zero' at reverse biases (shown in Figure S11) and thus good asymmetry is observed whether Schottky currents are considered or not. However, for larger $\psi_R - \psi_L$ the reverse Schottky current exhibits a higher 'near zero' value than the reverse tunneling current and therefore results in a reduction of the asymmetry (where tunneling current is dominant in the forward bias) as shown in Figure S13 in the supplementary material. These asymmetry results present two cases, one where reverse tunneling current dominates and the other where Schottky reverse current dominates. Experimentally, the actual diode asymmetry is likely to fall between the two. Experimental investigation is warranted to further observe the influence of tunneling and Schottky dominated reverse currents on the FOM of MIM diodes with insulator tuning.

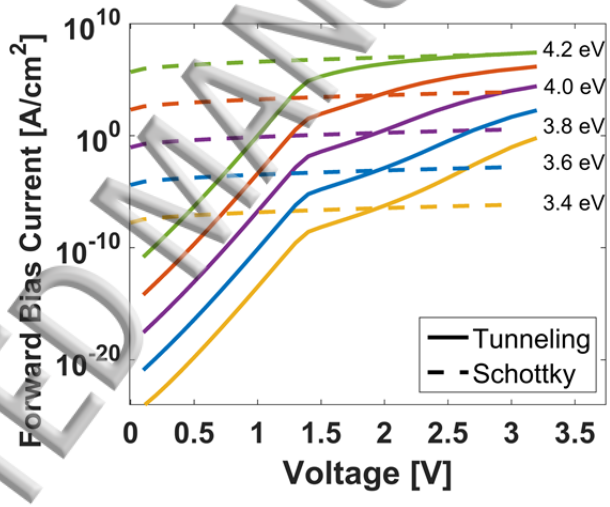

FIG. 8 Comparison of Schottky (dashed) and tunneling current (solid) of 6nm thick Al-TiO_2-Pl diode with increasing electron affinity (3.4eV to 4.2eV). The Schottky current is dominant at low bias before the turn on bias of the tunneling current, after which tunneling current dominates. Schottky current is prevalent at high electron affinities where the potential barrier height is low, as observed for the χ_A =4.2eV current. Figure S11 in the supplementary material further shows the magnitude difference between Schottky and tunneling currents for $\chi_A = 3.6eV, 3.8eV, 4.0eV, 4.2eV$.

Poole-Frenkel emission is dependent on the energy levels and quantity of random trap states in the insulator that occur due to defects or impurities. It has been classified as a bulk conduction process and has a thickness dependence[74,99]. PF emissions have been found to be the dominant conduction process for a few reported MIM diodes with undoped insulators[17,18,100], which suggest that insulator materials are defective to begin with in regards to trap states. A study by Lenz *et al*, on the charge transport mechanisms of doped nanoparticle thin films concluded that PF emissions are tied to the

intrinsic defects of the material, such that extrinsic effects from doping do not significantly alter the film's conduction process[101]. A report by Schroeder has cast an element of doubt in verifying PF conduction, stating the effects of PF are "negligibly small" in MIM stacks[102]. PF emission is not easily modeled as the energy levels of the random trap states are required to be known[75], but its potential impact on the simulations presented in this work can be discussed qualitatively. When the electron affinity is tuned by insulator doping, the introduction of impurities may result in PF emissions becoming a dominant conduction process over tunnelling. This may be prevalent when χ_A is tuned over a large range and a considerable amount of dopant atoms are introduced, increasing the defect density and the number of trap states available for conduction. This would result in an increase in current density in both directions through the diode, largely symmetric IV curves[18], and a decrease in the diode FOM, notably asymmetry. However, the FOM results presented herein (Figure 6 and 7) have only considered slight χ_A tuning of ±0.2eV. For these small changes in electron affinity, the defect density is not expected to change significantly, particularly given the defective nature of undoped insulators noted above, and thus not have a large impact on the FOM.

Tuning of the insulator electron affinity is likely to change other properties of the layer which may also influence the performance of the diode. The introduction of dopant atoms will change the mobility of electrons and increase the probability of scattering events influencing the conductivity of the material[103]. Doping of thin films can alter the dielectric constant[104] which will affect the diode capacitance and accordingly the cut-off frequency. The change in these properties may have an impact on the diode FOM, and while they are beyond the scope of this work, they similarly warrant experimental investigation.

IV. CONCLUSION

Previous efforts to improve the MIM diode figures of merit have often been at the expense of increasing the diode resistance and hence limiting the operating frequency. The effect of tuning the electron affinity of the insulator layer of a MIM diode was investigated using an Airy Function Transfer Matrix simulation method as a possible technique to decrease the diode resistance while maintaining good figures of merit. Furthermore, the simulation study observed the effect of insulator thickness and the selection of metals in conjunction with increasing electron affinity on the diode IV characteristic and FOM values. Tuning of the electron affinity allows for lowering of the potential barrier height to facilitate electron tunnelling and therefore lowers resistance. A key point is that the barrier height is adjusted on both sides the barrier, while preserving its profile given by the insulator thickness and metal work functions. Consequently, it was found that the decrease in resistance obtained by electron affinity tuning is sensitive to the thickness and $\psi_R - \psi_L$. For thicker diodes (6-10 nm), it was shown that a slight increase in electron affinity (0.2 eV) can decrease the diode resistance by a potential five orders of

magnitude, resulting in a concomitant increase in the operating frequency. The effect of increasing electron affinity on the diode asymmetry was also simulated. An improved asymmetry was observed for thinner diodes (approximately an order of magnitude improvement for diodes with large electrode work function differences), with negligible change observed for thicker diodes. Relatively small decreases in nonlinearity and responsivity were observed when the insulator's electron affinity was increased. Alternative Schottky and Poole-Frenkel conduction processes and their potential impact on the diode FOM were also considered. Schottky conduction is expected to be significant at high electron affinities resulting in a reduction in the FOM. The influence of Poole-Frenkel conduction is expected to be negligible for the case of small χ_A tuning but may become significant in the case of large χ_A tuning. The simulations performed in this work indicate that tuning of the insulator electron affinity (e.g., by doping) is a feasible technique to increase the operating frequency of MIM diodes closer to terahertz rectification while maintaining good figures of merit. Experimental effects that are liable to influence diode performance were noted and the need to verify these simulations through experimental investigation was highlighted.

SUPPLEMENTARY MATERIAL

See Supplementary Material for additional simulation results as discussed in main text.

REFERENCES

1. Azad, I., Ram, M. K., Goswami, D. Y. & Stefanakos, E. Au/Cr-ZnO-Ni structured metal-insulator-metal diode fabrication using Langmuir-Blodgett technique for infrared sensing. in *Infared Technology and Applications XLII* (eds. Andresen, B. F., Fulop, G. F., Hanson, C. M., Miller, J. L. & Norton, P. R.) **9819,** 98190E (SPIE, 2016).

2. Gadalla, M. N., Abdel-Rahman, M. & Shamim, A. Design, Optimization and Fabrication of a 28.3 THz Nano-Rectenna for Infrared Detection and Rectification. *Sci. Rep.* **4,** 79–85 (2014).

3. Donchev, E., Pang, J. S., Gammon, P. M., Centeno, A., Xie, F., Petrov, P. K., Breeze, J. D., Ryan, M. P., Riley, D. J. & Alford, N. M. The rectenna device: From theory to practice (a review). *MRS Energy Sustain.* **1,** E1 (2014).

4. Bhatt, K. & Tripathi, C. C. Comparative analysis of efficient diode design for terahertz wireless power transmission system. *Indian J. Pure Appl. Phys.* **53,** 827–836 (2015).

5. Inac, M., Shafique, A., Ozcan, M. & Gurbuz, Y. Device characteristics of antenna-coupled metal-insulator-metal diodes (rectenna) using Al2O3 , TiO2 , and Cr2O3 as insulator layer for energy harvesting applications. in *Thin Films for Solar and Energy Technology VII* (eds. Eldada, L. A. & Heben, M. J.) **9561,** 95610M (SPIE, 2015).

6. Periasamy, P. & O'Hayre, R. P. G. D. S. Metal-insulator-metal diodes towards THz and optical energy harvesting: Development of materials design principles. 3552634, (Colorado School of Mines, 2013).

7. Blake J. Eliasson. Metal Insulator Metal Diodes For Solar Energy Conversion. (University of Colorado, 2001).

8. Periasamy, P., Guthrey, H. L., Abdulagatov, A. I., Ndione, P. F., Berry, J. J., Ginley, D. S., George, S. M., Parilla, P. A. & O'Hayre, R. P. Metal-Insulator-Metal Diodes: Role of the Insulator Layer on the Rectification Performance. *Adv. Mater.* **25,** 1301–1308 (2013).

9. Periasamy, P., Berry, J. J., Dameron, A. a, Bergeson, J. D., Ginley, D. S., O'Hayre, R. P. & Parilla, P. a. Fabrication and Characterization of MIM Diodes Based on Nb/Nb2O5 Via a Rapid Screening Technique. *Adv. Mater.* **23,** 3080–3085 (2011).

10. Shin, J. H., Im, J., Choi, J.-W., Kim, H. S., Sohn, J. I., Cha, S. N. & Jang, J. E. Ultrafast metal-insulator-multi-wall carbon nanotube tunneling diode employing asymmetrical structure effect. *Carbon N. Y.* **102,** 172–180 (2016).

11. Liu, H., Chen, B., Li, X., Liu, W., Ding, Y. & Lu, B. A metal/insulator/metal field-emission cannon. *Nanotechnology* **22,** 455302 (2011).

12. Ftor, D., Dodd, L. E., Wood, D. & Palovcak, A. Metal-insulator-metal diodes fabricated on flexible substrates. in *2016 41st International Conference on Infrared, Millimeter, and Terahertz waves (IRMMW-THz)* 1–2 (IEEE, 2016). doi:10.1109/IRMMW-THz.2016.7758643

13. Maraghechi, P., Foroughi-Abari, A., Cadien, K. & Elezzabi, A. Y. Enhanced rectifying response from metal-insulator-insulator-metal junctions. *Appl. Phys. Lett.* **99,** 253503 (2011).

14. Zhuang, C., Wang, L., Dai, Z. & Yang, D. High Frequency Ni-NiO-Ag Metal-Insulator-Metal Tunnel Diodes Fabricated via Anodic Aluminum Oxide Templates. *ECS Solid State Lett.* **4,** P39–P42 (2015).

15. Grover, S. & Moddel, G. Engineering the current–voltage characteristics of metal–insulator–metal diodes using double-insulator tunnel barriers. *Solid. State. Electron.* **67,** 94–99 (2012).

16. Hashem, I. E., Rafat, N. H. & Soliman, E. a. Theoretical Study of Metal-Insulator-Metal Tunneling Diode Figures of Merit. *IEEE J. Quantum Electron.* **49,** 72–79 (2013).

17. Alimardani, N., King, S. W., French, B. L., Tan, C., Lampert, B. P. & Conley, J. F. Investigation of the impact of insulator material on the performance of dissimilar electrode metal-insulator-metal diodes. *J. Appl. Phys.* **116,** 24508 (2014).

18. Alimardani, N., McGlone, J. M., Wager, J. F. & Conley, J. F. Conduction processes in metal–insulator–metal diodes with Ta 2 O 5 and Nb 2 O 5 insulators deposited by atomic layer deposition. *J. Vac. Sci. Technol. A Vacuum, Surfaces, Film.* **32,** 01A122 (2014).

19. Grover, S. & Moddel, G. Applicability of Metal/Insulator/Metal (MIM) Diodes to Solar Rectennas. *IEEE J. Photovoltaics* **1,** 78–83 (2011).

20. Hoye, R. L. Z., Ehrler, B., Böhm, M. L., Muñoz-Rojas, D., Altamimi, R. M., Alyamani, A. Y., Vaynzof, Y., Sadhanala, A., Ercolano, G., Greenham, N. C., Friend, R. H., MacManus-Driscoll, J. L. & Musselman, K. P. Improved Open- Circuit Voltage in ZnO-PbSe Quantum Dot Solar Cells by Understanding and Reducing Losses Arising from the ZnO Conduction Band Tail. *Adv. Energy Mater.* **4,** 1301544 (2014).

21. Hamberg, I., Granqvist, C. G., Berggren, K. F., Sernelius, B. E. & Engström, L. Band-gap widening in heavily Sn-doped In2O3. *Phys. Rev. B* **30,** 3240–3249 (1984).

22. Sernelius, B. E., Berggren, K.-F., Jin, Z.-C., Hamberg, I. & Granqvist, C. G. Band-gap tailoring of ZnO by means of heavy Al doping. *Phys. Rev. B* **37,** 10244–10248 (1988).

23. Sanon, G., Rup, R. & Mansingh, A. Band-gap narrowing and band structure in degenerate tin oxide (SnO2) films. *Phys. Rev. B* **44,** 5672–5680 (1991).

24. Jain, A., Sagar, P. & Mehra, R. M. Band gap widening and narrowing in moderately and heavily doped n-ZnO films. *Solid. State. Electron.* **50,** 1420–1424 (2006).

25. Lu, J. G., Fujita, S., Kawaharamura, T., Nishinaka, H., Kamada, Y., Ohshima, T., Ye, Z. Z., Zeng, Y. J., Zhang, Y. Z., Zhu, L. P., He, H. P. & Zhao, B. H. Carrier concentration dependence of band gap shift in n-type ZnO:Al films. *J. Appl. Phys.* **101,** 83705 (2007).

26. Nakano, Y., Saeki, S. & Morikawa, T. Optical bandgap widening of p-type Cu2O films by nitrogen doping. *Appl. Phys. Lett.* **94,** 22111 (2009).

27. Gupta, L., Mansingh, A. & Srivastava, P. K. Band gap narrowing and the band structure of tin-doped indium oxide films. *Thin Solid Films* **176,** 33–44 (1989).

28. Gupta, R. K., Yakuphanoglu, F. & Amanullah, F. M. Band gap engineering of nanostructure Cu doped CdO films. *Phys. E Low-Dimensional Syst. Nanostructures* **43,** 1666–1668 (2011).

29. Hoye, R. L. Z., Muñoz-Rojas, D., Nelson, S. F., Illiberi, A., Poodt, P., Roozeboom, F. & MacManus-Driscoll, J. L. Research Update: Atmospheric pressure spatial atomic layer deposition of ZnO thin films: Reactors, doping, and devices. *APL Mater.* **3,** 40701 (2015).

30. Banerjee, P., Lee, W.-J., Bae, K.-R., Lee, S. B. & Rubloff, G. W. Structural, electrical, and optical properties of atomic layer deposition Al-doped ZnO films. *J. Appl. Phys.* **108,** 43504 (2010).

31. Lim, S. J., Kwon, S., Kim, H. & Park, J.-S. High performance thin film transistor with low temperature atomic layer deposition nitrogen-doped ZnO. *Appl. Phys. Lett.* **91,** 183517 (2007).

32. Yang, J. J., Kobayashi, N. P., Strachan, J. P., Zhang, M.-X., Ohlberg, D. A. A., Pickett, M. D., Li, Z., Medeiros-Ribeiro, G. & Williams, R. S. Dopant Control by Atomic Layer Deposition in Oxide Films for Memristive Switches. *Chem. Mater.* **23,** 123–125 (2011).

33. Lee, D.-J., Kim, K.-J., Kim, S.-H., Kwon, J.-Y., Xu, J. & Kim, K.-B. Atomic layer deposition of Ti-doped ZnO films with enhanced electron mobility. *J. Mater. Chem. C* **1,** 4761 (2013).

34. Minami, T., Yamamoto, T. & Miyata, T. Highly transparent and conductive rare earth-doped ZnO thin films prepared

by magnetron sputtering. *Thin Solid Films* **366,** 63–68 (2000).

35. Minami, T., Nanto, H. & Takata, S. Highly Conductive and Transparent Aluminum Doped Zinc Oxide Thin Films Prepared by RF Magnetron Sputtering. *Jpn. J. Appl. Phys.* **23,** L280–L282 (1984).

36. Minami, T., Sato, H., Nanto, H. & Takata, S. Group III Impurity Doped Zinc Oxide Thin Films Prepared by RF Magnetron Sputtering. *Jpn. J. Appl. Phys.* **24,** L781–L784 (1985).

37. Ohshima, T., Maeda, T., Tanaka, Y., Kawasaki, H., Yagyu, Y., Ihara, T. & Suda, Y. Sputtering deposition of Al-doped zinc oxide thin films using mixed powder targets. *Jpn. J. Appl. Phys.* **55,** 01AA08 (2016).

38. Sathasivam, S., Bhachu, D. S., Lu, Y., Chadwick, N., Althabaiti, S. A., Alyoubi, A. O., Basahel, S. N., Carmalt, C. J. & Parkin, I. P. Tungsten Doped TiO2 with Enhanced Photocatalytic and Optoelectrical Properties via Aerosol Assisted Chemical Vapor Deposition. *Sci. Rep.* **5,** 10952 (2015).

39. Kafizas, A., Noor, N., Carmichael, P., Scanlon, D. O., Carmalt, C. J. & Parkin, I. P. Combinatorial Atmospheric Pressure Chemical Vapor Deposition of F:TiO 2 ; the Relationship between Photocatalysis and Transparent Conducting Oxide Properties. *Adv. Funct. Mater.* **24,** 1758–1771 (2014).

40. Giordano, F., Abate, A., Correa Baena, J. P., Saliba, M., Matsui, T., Im, S. H., Zakeeruddin, S. M., Nazeeruddin, M. K., Hagfeldt, A. & Graetzel, M. Enhanced electronic properties in mesoporous TiO2 via lithium doping for high-efficiency perovskite solar cells. *Nat. Commun.* **7,** 10379 (2016).

41. Yamauchi, S., Saiki, S., Ishibashi, K., Nakagawa, A. & Hatakeyama, S. Low Pressure Chemical Vapor Deposition of Nb and F Co-Doped TiO2 Layer. *J. Cryst. Process Technol.* **4,** 79–88 (2014).

42. Hu, J. & Gordon, R. G. Textured fluorine-doped ZnO films by atmospheric pressure chemical vapor deposition and their use in amorphous silicon solar cells. *Sol. Cells* **30,** 437–450 (1991).

43. Heikman, S., Keller, S., DenBaars, S. P. & Mishra, U. K. Growth of Fe doped semi-insulating GaN by metalorganic chemical vapor deposition. *Appl. Phys. Lett.* **81,** 439–441 (2002).

44. Wei, D., Liu, Y., Wang, Y., Zhang, H., Huang, L. & Yu, G. Synthesis of N-Doped Graphene by Chemical Vapor Deposition and Its Electrical Properties. *Nano Lett.* **9,** 1752–1758 (2009).

45. Hu, J. & Gordon, R. G. Textured aluminum□doped zinc oxide thin films from atmospheric pressure chemical□vapor deposition. *J. Appl. Phys.* **71,** 880–890 (1992).

46. Götz, W., Johnson, N. M., Walker, J., Bour, D. P. & Street, R. A. Activation of acceptors in Mg doped GaN grown by metalorganic chemical vapor deposition. *Appl. Phys. Lett.* **68,** 667–669 (1996).

47. Baniecki, J. D., Yamazaki, T., Ricinschi, D., Van Overmeere, Q., Aso, H., Miyata, Y., Yamada, H., Fujimura, N., Maran, R., Anazawa, T., Valanoor, N. & Imanaka, Y. Strain Dependent Electronic Structure and Band Offset Tuning at Heterointerfaces of ASnO3 (A=Ca, Sr, and Ba) and SrTiO3. *Sci. Rep.* **7,** 41725 (2017).

48. Singh, D. J., Xu, Q. & Ong, K. P. Strain effects on the band gap and optical properties of perovskite SrSnO 3 and BaSnO 3. *Appl. Phys. Lett.* **104,** 11910 (2014).

49. Chambers, S. A., Kaspar, T. C., Prakash, A., Haugstad, G. & Jalan, B. Band alignment at epitaxial BaSnO 3 /SrTiO 3 (001) and BaSnO 3 /LaAlO 3 (001) heterojunctions. *Appl. Phys. Lett.* **108,** 152104 (2016).

50. Berger, R. F., Fennie, C. J. & Neaton, J. B. Band Gap and Edge Engineering via Ferroic Distortion and Anisotropic Strain: The Case of SrTiO3. *Phys. Rev. Lett.* **107,** 146804 (2011).

51. Li, H., Castelli, I. E., Thygesen, K. S. & Jacobsen, K. W. Strain sensitivity of band gaps of Sn-containing semiconductors. *Phys. Rev. B* **91,** 45204 (2015).

52. Johari, P. & Shenoy, V. B. Tuning the Electronic Properties of Semiconducting Transition Metal Dichalcogenides by Applying Mechanical Strains. *ACS Nano* **6,** 5449–5456 (2012).

53. Zhang, Z., Wang, J., Song, C., Mao, H. & Zhao, Q. Tuning Band Gaps of Transition Metal Dichalcogenides WX2 (X = S, Se) Nanoribbons by External Strain. *J. Nanosci. Nanotechnol.* **16,** 8090–8095 (2016).

54. Ram, B., Manjanath, A. & Singh, A. K. From semiconductor to metal: A reversible tuning of electronic properties of mono to multilayered SnS2 under applied strain. (2015).

55. Smith, A. M., Mohs, A. M. & Nie, S. Tuning the optical and electronic properties of colloidal nanocrystals by lattice strain. *Nat. Nanotechnol.* **4,** 56–63 (2009).

56. Khatun, N., Rini, E. G., Shirage, P., Rajput, P., Jha, S. N. & Sen, S. Effect of lattice distortion on bandgap decrement due to vanadium substitution in TiO2 nanoparticles. *Mater. Sci. Semicond. Process.* **50,** 7–13 (2016).

57. Filip, M. R., Eperon, G. E., Snaith, H. J. & Giustino, F. Steric engineering of metal-halide perovskites with tunable optical band gaps. *Nat. Commun.* **5,** 5757 (2014).

58. Balachandran, P. V & Rondinelli, J. M. Massive band gap variation in layered oxides through cation ordering. *Nat.*

Commun. **6,** 6191 (2015).

59. Amat, A., Mosconi, E., Ronca, E., Quarti, C., Umari, P., Nazeeruddin, M. K., Grätzel, M. & De Angelis, F. Cation-Induced Band-Gap Tuning in Organohalide Perovskites: Interplay of Spin–Orbit Coupling and Octahedra Tilting. *Nano Lett.* **14,** 3608–3616 (2014).

60. Yin, W.-J., Chen, S., Yang, J.-H., Gong, X.-G., Yan, Y. & Wei, S.-H. Effective band gap narrowing of anatase TiO2 by strain along a soft crystal direction. *Appl. Phys. Lett.* **96,** 221901 (2010).

61. Rus, S. F., Ward, T. Z. & Herklotz, A. Strain-induced optical band gap variation of SnO2 films. *Thin Solid Films* **615,** 103–106 (2016).

62. Suzuki, T., Watanabe, H., Oaki, Y. & Imai, H. Tuning of photocatalytic reduction by conduction band engineering of semiconductor quantum dots with experimental evaluation of the band edge potential. *Chem. Commun.* **52,** 6185–6188 (2016).

63. Kongkanand, A., Tvrdy, K., Takechi, K., Kuno, M. & Kamat, P. V. Quantum Dot Solar Cells. Tuning Photoresponse through Size and Shape Control of CdSe−TiO 2 Architecture. *J. Am. Chem. Soc.* **130,** 4007–4015 (2008).

64. Chuang, C.-H. M., Brown, P. R., Bulović, V. & Bawendi, M. G. Improved performance and stability in quantum dot solar cells through band alignment engineering. *Nat. Mater.* **13,** 796–801 (2014).

65. Baskoutas, S. & Terzis, A. F. Size-dependent band gap of colloidal quantum dots. *J. Appl. Phys.* **99,** 13708 (2006).

66. Lu, J. G., Ye, Z. Z., Zhang, Y. Z., Liang, Q. L., Fujita, S. & Wang, Z. L. Self-assembled ZnO quantum dots with tunable optical properties. *Appl. Phys. Lett.* **89,** 4–6 (2006).

67. Lin, K.-F., Cheng, H.-M., Hsu, H.-C., Lin, L.-J. & Hsieh, W.-F. Band gap variation of size-controlled ZnO quantum dots synthesized by sol–gel method. *Chem. Phys. Lett.* **409,** 208–211 (2005).

68. Lin, H., Huang, C., Li, W., Ni, C., Shah, S. & Tseng, Y. Size dependency of nanocrystalline TiO2 on its optical property and photocatalytic reactivity exemplified by 2-chlorophenol. *Appl. Catal. B Environ.* **68,** 1–11 (2006).

69. Lee, H., Woo, C., Youn, B., Kim, S., Oh, S., Sung, Y. & Lee, H. Bandgap modulation of TiO 2 and its effect on the activity in photocatalytic oxidation of 2-isopropyl-6-methyl-4-pyrimidinol. *Top. Catal.* **35,** 255–260 (2005).

70. Brown, P. R., Kim, D., Lunt, R. R., Zhao, N., Bawendi, M. G., Grossman, J. C. & Bulović, V. Energy Level Modification in Lead Sulfide Quantum Dot Thin Films through Ligand Exchange. *ACS Nano* **8,** 5863–5872 (2014).

71. Cao, D., Liu, Q., Zeng, W., Yuan, S., Peng, J. & Lu, S. Diketopyrrolopyrrole-Containing Polyfluorenes: Facile Method To Tune Emission Color and Improve Electron Affinity. *Macromolecules* **39,** 8347–8355 (2006).

72. Meyers, F., Heeger, A. J. & Brédas, J. L. Fine tuning of the band gap in conjugated polymers via control of block copolymer sequences. *J. Chem. Phys.* **97,** 2750–2758 (1992).

73. Peng, Q., Park, K., Lin, T., Durstock, M. & Dai, L. Donor-π-Acceptor Conjugated Copolymers for Photovoltaic Applications: Tuning the Open-Circuit Voltage by Adjusting the Donor/Acceptor Ratio. *J. Phys. Chem. B* **112,** 2801–2808 (2008).

74. Simmons, J. G. Conduction in thin dielectric films. *J. Phys. D. Appl. Phys.* **4,** 202 (1971).

75. Chiu, F. A Review on Conduction Mechanisms in Dielectric Films. *Adv. Mater. Sci. Eng.* **2014,** 1–18 (2014).

76. Fowler, R. H. & Nordheim, L. Electron Emission in Intense Electric Fields. *Proc. R. Soc. London A Math. Phys. Eng. Sci.* **119,** (1928).

77. Ajayi, O. A. DC and RF Characterization of High Frequency ALD Enhanced Nanostructured Metal-Insulator- Metal Diodes. (University of South Florida, 2014).

78. Simmons, J. G. Generalized Formula for the Electric Tunnel Effect between Similar Electrodes Separated by a Thin Insulating Film. *J. Appl. Phys.* **34,** 1793–1803 (1963).

79. Probst, O. M. Tunneling through arbitrary potential barriers and the apparent barrier height. *Am. J. Phys.* **70,** 1110–1116 (2002).

80. Cowell, E. W., Muir, S. W., Keszler, D. A. & Wager, J. F. Barrier height estimation of asymmetric metal-insulator-metal tunneling diodes. *J. Appl. Phys.* **114,** 213703 (2013).

81. Singh, A., Ratnadurai, R., Kumar, R., Krishnan, S., Emirov, Y. & Bhansali, S. Fabrication and current–voltage characteristics of NiOx/ZnO based MIIM tunnel diode. *Appl. Surf. Sci.* **334,** 197–204 (2015).

82. Brinkman, W. F., Dynes, R. C. & Rowell, J. M. Tunneling Conductance of Asymmetrical Barriers. *J. Appl. Phys.* **41,** 1915–1921 (1970).

83. Hashem, I. E., Rafat, N. H. & Soliman, E. A. Characterization of MIM Diodes based on Nb/ Nb 2 O 5. in *IEEE 5Th International Nanoelectronics Conference (INEC)* (2013).

84. Aydinoglu, F., Alhazmi, M., Cui, B., Om, R. & Irannejad, M. Higher Performance Metal-Insulator-Metal Diodes

using Multiple Insulator Layers. *Adapt. Nanoappedtive Nanotechnol.* **1,** 3–5 (2014).

85. Umebayashi, T., Yamaki, T., Itoh, H. & Asai, K. Band gap narrowing of titanium dioxide by sulfur doping. *Appl. Phys. Lett.* **81,** 454–456 (2002).

86. Di Valentin, C., Pacchioni, G. & Selloni, A. Theory of Carbon Doping of Titanium Dioxide. *Chem. Mater.* **17,** 6656–6665 (2005).

87. LIU, Y., WANG, H. & WU, Z. Characterization of metal doped-titanium dioxide and behaviors on photocatalytic oxidation of nitrogen oxides. *J. Environ. Sci.* **19,** 1505–1509 (2007).

88. Zaleska, A. Doped-TiO2: A Review. *Recent Patents Eng.* **2,** 157–164 (2008).

89. Asahi, R., Morikawa, T., Irie, H. & Ohwaki, T. Nitrogen-Doped Titanium Dioxide as Visible-Light-Sensitive Photocatalyst: Designs, Developments, and Prospects. *Chem. Rev.* **114,** 9824–9852 (2014).

90. Ortiz-Conde, A., García Sánchez, F. J., Liou, J. J., Cerdeira, A., Estrada, M. & Yue, Y. A review of recent MOSFET threshold voltage extraction methods. *Microelectron. Reliab.* **42,** 583–596 (2002).

91. Alimardani, N., William Cowell, E., Wager, J. F., Conley, J. F., Evans, D. R., Chin, M., Kilpatrick, S. J. & Dubey, M. Impact of electrode roughness on metal-insulator-metal tunnel diodes with atomic layer deposited Al 2 O 3 tunnel barriers. *J. Vac. Sci. Technol. A Vacuum, Surfaces, Film.* **30,** 01A113 (2012).

92. Miller, C. W., Li, Z.-P., Åkerman, J. & Schuller, I. K. Impact of interfacial roughness on tunneling conductance and extracted barrier parameters. *Appl. Phys. Lett.* **90,** 43513 (2007).

93. Magno, R., Bracker, A. S., Bennett, B. R., Nosho, B. Z. & Whitman, L. J. Barrier roughness effects in resonant interband tunnel diodes. *J. Appl. Phys.* **90,** 6177–6181 (2001).

94. Cowell, E. W., Alimardani, N., Knutson, C. C., Conley, J. F., Keszler, D. A., Gibbons, B. J. & Wager, J. F. Advancing MIM Electronics: Amorphous Metal Electrodes. *Adv. Mater.* **23,** 74–78 (2011).

95. Choi, K., Yesilkoy, F., Ryu, G., Cho, S. H., Goldsman, N., Dagenais, M. & Peckerar, M. A Focused Asymmetric Metal-Insulator-Metal Tunneling Diode: Fabrication, DC Characteristics and RF Rectification Analysis. *IEEE Trans. Electron Devices* **58,** 3519–3528 (2011).

96. Grubbs, M. E., Zhang, X., Deal, M., Nishi, Y. & Clemens, B. M. Development and characterization of high temperature stable Ta–W–Si–C amorphous metal gates. *Appl. Phys. Lett.* **97,** 223505 (2010).

97. Usui, T., Mollinger, S. A., Ianca, V. P. S., Reis, R. M. & Primit, K. B. High aspect ratio and high breakdown strength metal-oxide capacitors. *Appl. Phys. Lett.* **101,** 33905 (2012).

98. George, S. M. Atomic Layer Deposition: An Overview. *Chem. Rev.* **110,** 111–131 (2010).

99. Simmons, J. G. Transition from Electrode-Limited to Bulk-Limited Conduction Processes in Metal-Insulator-Metal Systems. *Phys. Rev.* **166,** 912–920 (1968).

100. Alimardani, N. & Conley, J. F. Enhancing metal-insulator-insulator-metal tunnel diodes via defect enhanced direct tunneling. *Appl. Phys. Lett.* **105,** 82902 (2014).

101. Lenz, T., Richter, M., Matt, G. J., Luechinger, N. A., Halim, S. C., Heiss, W. & Brabec, C. J. Charge transport in nanoparticular thin films of zinc oxide and aluminum-doped zinc oxide. *J. Mater. Chem. C* **3,** 1468–1472 (2015).

102. Schroeder, H. Poole-Frenkel-effect as dominating current mechanism in thin oxide films—An illusion?! *J. Appl. Phys.* **117,** 215103 (2015).

103. Nunes, P., Fortunato, E., Tonello, P., Braz Fernandes, F., Vilarinho, P. & Martins, R. Effect of different dopant elements on the properties of ZnO thin films. *Vacuum* **64,** 281–285 (2002).

104. Fischer, D. & Kersch, A. The effect of dopants on the dielectric constant of HfO2 and ZrO2 from first principles. *Appl. Phys. Lett.* **92,** 12908 (2008).

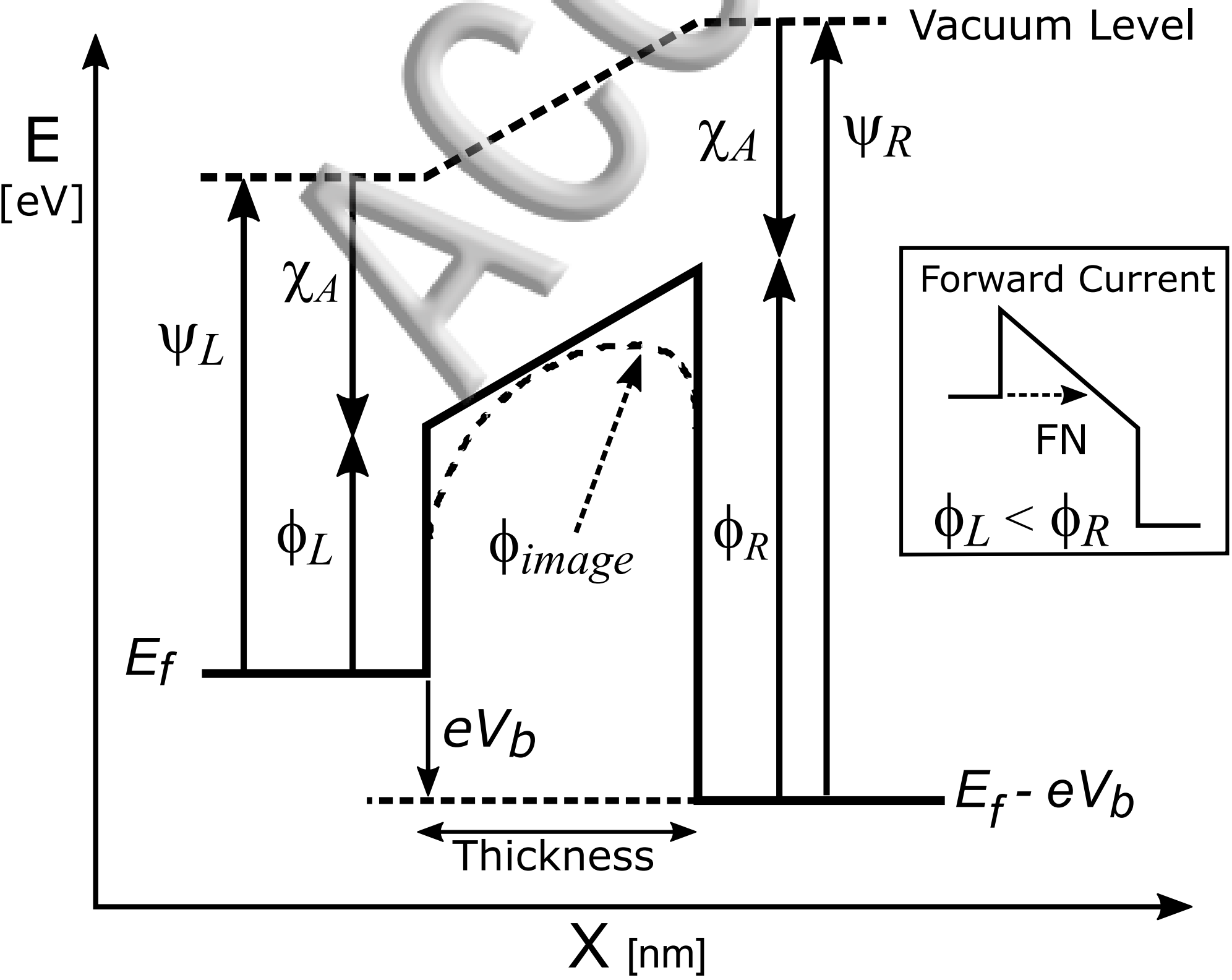
Vacuum Level
E
[eV]
χ_A
ψ_R
χ_A
ψ_L
Forward Current
FN
$\phi_L < \phi_R$
ϕ_L
ϕ_{image}
ϕ_R
E_f
eV_b
E_f - eV_b
Thickness
X [nm]

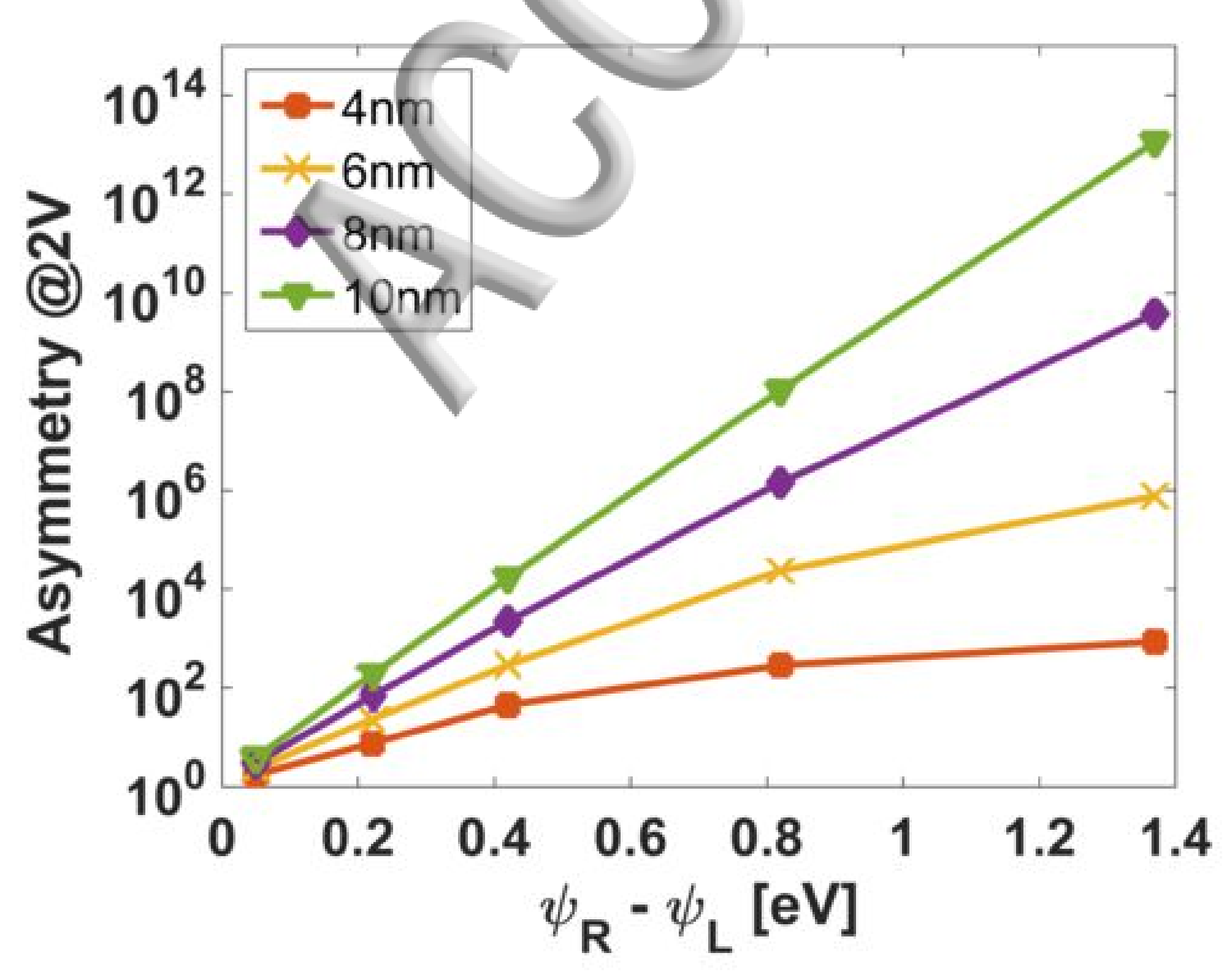
4nm
6nm
8nm
10nm
Asymmetry @2V
10^{14}
10^{12}
10^{10}
10^{8}
10^{6}
10^{4}
10^{2}
10^{0}
0
0.2
0.4
0.6
0.8
1
1.2
1.4
$\psi_R - \psi_L$ [eV]

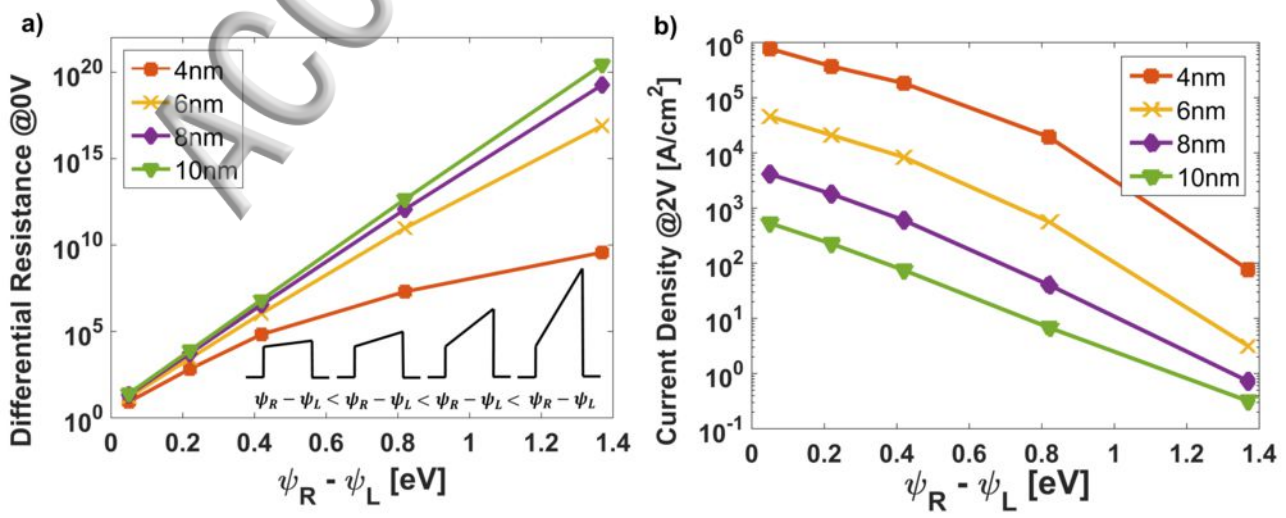
a)
Differential Resistance @0V
4nm
6nm
8nm
10nm
10^{20}
10^{15}
10^{10}
10^{5}
10^{0}
0
0.2
0.4
0.6
0.8
1
1.2
1.4
$\psi_R - \psi_L < \psi_R - \psi_L < \psi_R - \psi_L < \psi_R - \psi_L$
ψ_R - ψ_L [eV]
b)
Current Density @2V [A/cm^2]
4nm
6nm
8nm
10nm
10^{6}
10^{5}
10^{4}
10^{3}
10^{2}
10^{1}
10^{0}
10^{-1}
0
0.2
0.4
0.6
0.8
1
1.2
1.4
ψ_R - ψ_L [eV]

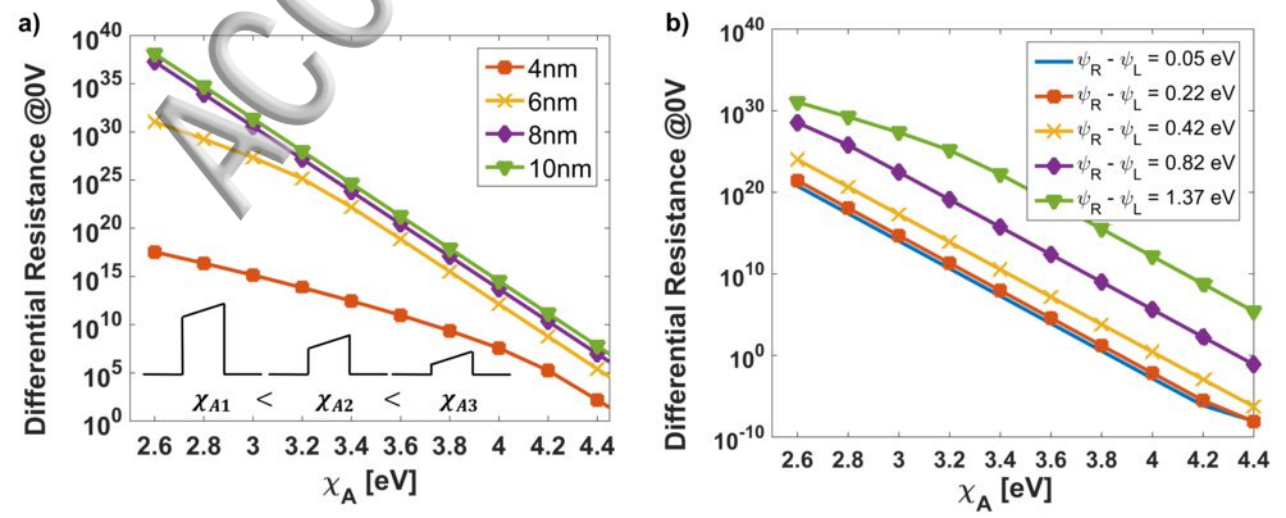
a)
Differential Resistance @0V
4nm
6nm
8nm
10nm
χ_{A1} < χ_{A2} < χ_{A3}
χ_A [eV]
b)
Differential Resistance @0V
ψ_R - ψ_L = 0.05 eV
ψ_R - ψ_L = 0.22 eV
ψ_R - ψ_L = 0.42 eV
ψ_R - ψ_L = 0.82 eV
ψ_R - ψ_L = 1.37 eV
χ_A [eV]

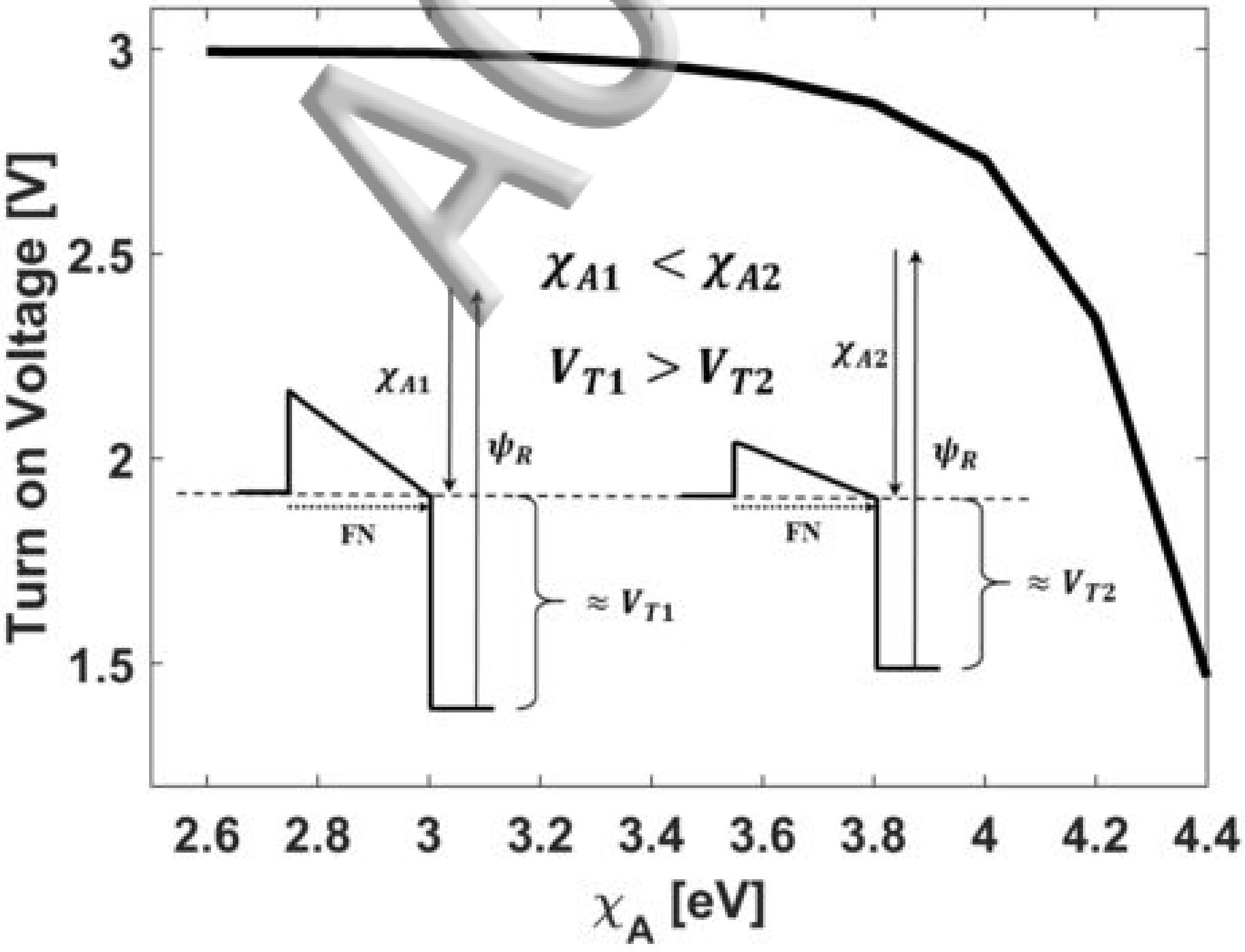
Turn on Voltage [V]
3
2.5
2
1.5
2.6
2.8
3
3.2
3.4
3.6
3.8
4
4.2
4.4
χ_A [eV]
$\chi_{A1} < \chi_{A2}$
$V_{T1} > V_{T2}$
χ_{A1}
χ_{A2}
ψ_R
ψ_R
FN
FN
$\approx V_{T1}$
$\approx V_{T2}$

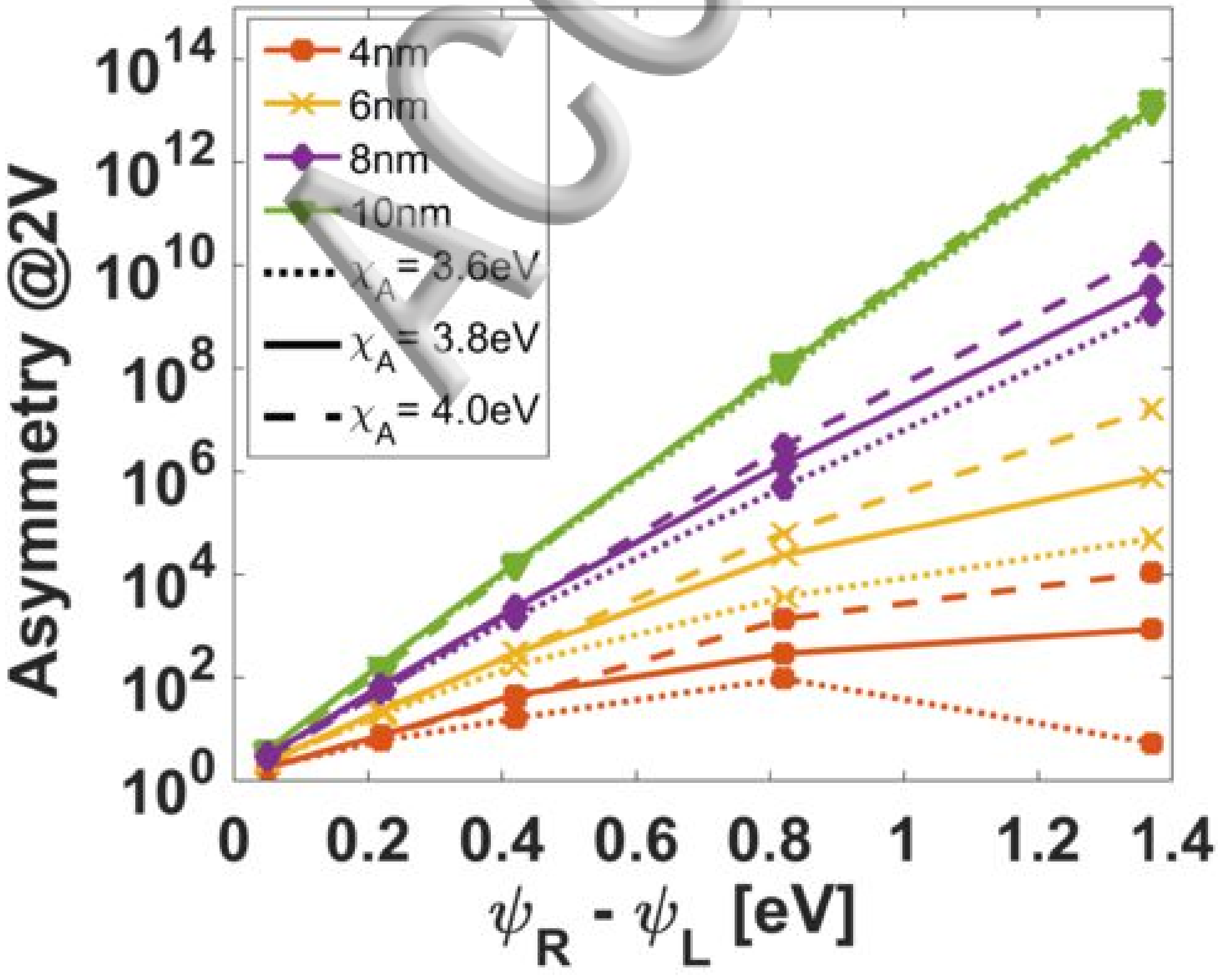
4nm
6nm
8nm
10nm
χ_A = 3.6eV
χ_A = 3.8eV
χ_A = 4.0eV
Asymmetry @2V
10^{14}
10^{12}
10^{10}
10^{8}
10^{6}
10^{4}
10^{2}
10^{0}
0
0.2
0.4
0.6
0.8
1
1.2
1.4
$\psi_R - \psi_L$ [eV]

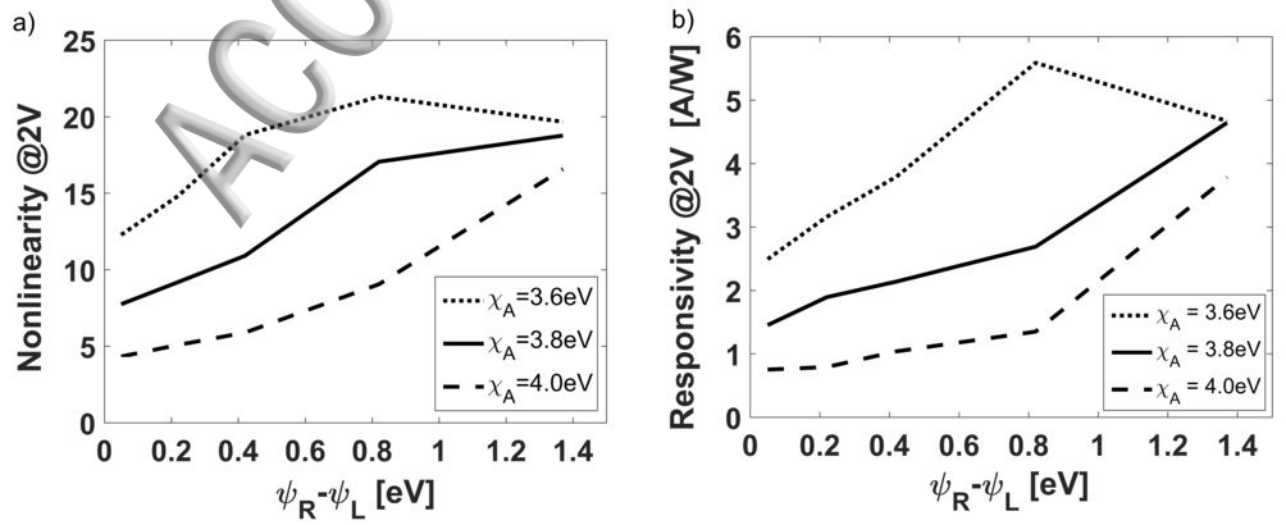
a)
Nonlinearity @2V
25
20
15
10
5
0
0
0.2
0.4
0.6
0.8
1
1.2
1.4
ψ_R-ψ_L [eV]
χ_A=3.6eV
χ_A=3.8eV
χ_A=4.0eV
b)
Responsivity @2V [A/W]
6
5
4
3
2
1
0
0
0.2
0.4
0.6
0.8
1
1.2
1.4
ψ_R-ψ_L [eV]
χ_A = 3.6eV
χ_A = 3.8eV
χ_A = 4.0eV

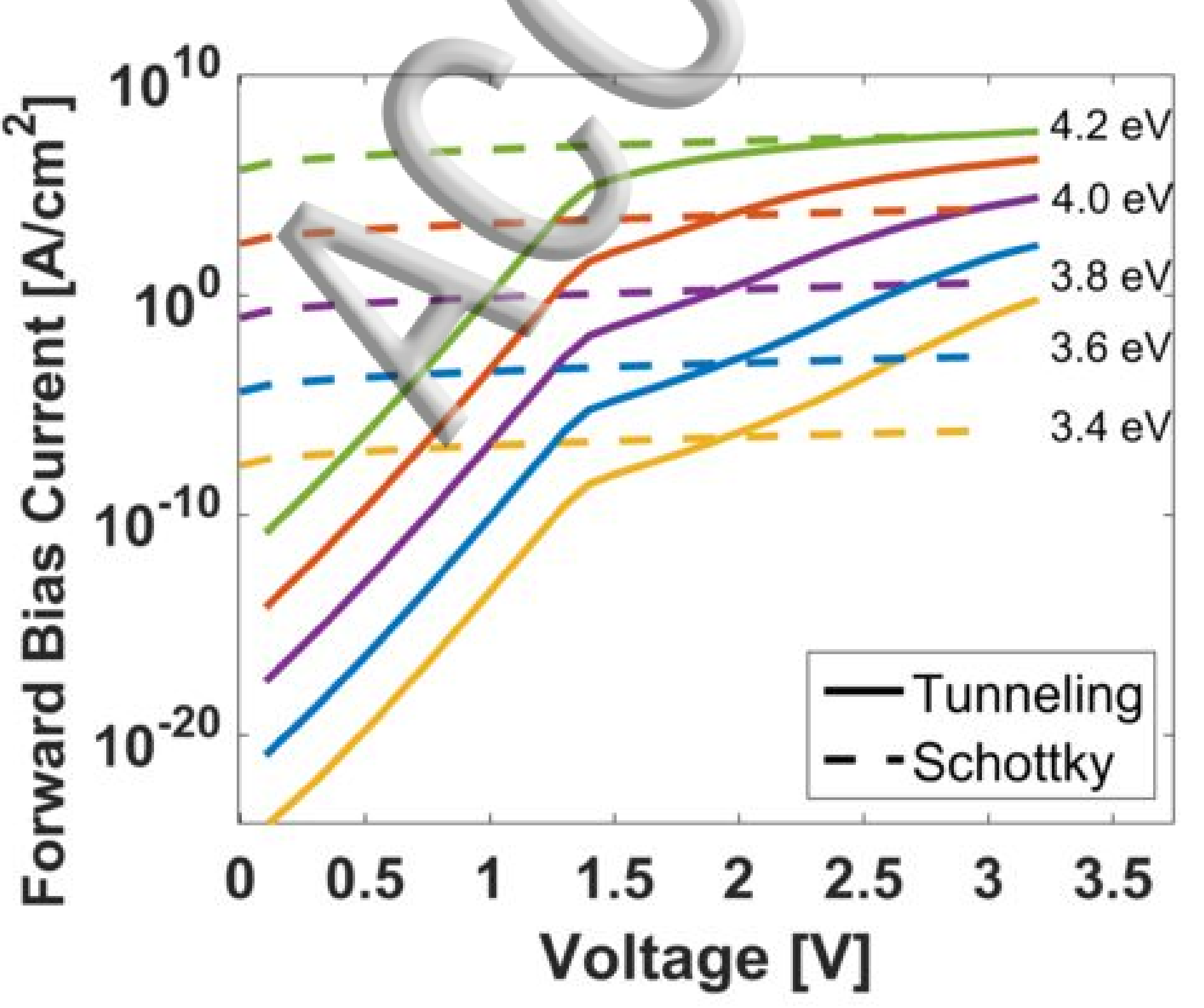
Forward Bias Current [A/cm^2]
10^{10}
10^{0}
10^{-10}
10^{-20}
4.2 eV
4.0 eV
3.8 eV
3.6 eV
3.4 eV
Tunneling
Schottky
0
0.5
1
1.5
2
2.5
3
3.5
Voltage [V]